Earth and Planetary Science Letters 415 (2015) 16–24

Contents lists available at ScienceDirect

Earth and Planetary Science Letters

www.elsevier.com/locate/epsl

Two crustal low-velocity channels beneath SE Tibet revealed by joint inversion of Rayleigh wave dispersion and receiver functions

Xuewei Bao [a,b,d], Xiaoxiao Sun [a,b,*], Mingjie Xu [a,b,*], David W. Eaton [d], Xiaodong Song [b,e], Liangshu Wang [a,b], Zhifeng Ding [c], Ning Mi [a,b], Hua Li [a,b], Dayong Yu [a,b], Zhouchuan Huang [a,b], Pan Wang [a,b]

[a] State Key Laboratory for Mineral Deposits Research, Nanjing University, Nanjing 210093, China
[b] Institute of Geophysics and Geodynamics, School of Earth Sciences and Engineering, Nanjing University, Nanjing, 210093, China
[c] Institute of Geophysics, China Earthquake Administration, No. 5 Minzuxueyuan Nanlu, Haidian District, Beijing, 100081, China
[d] Department of Geoscience, University of Calgary, 2500 University Drive NW, Calgary, AB, T2N 1N4, Canada
[e] Department of Geology, University of Illinois at Urbana–Champaign, IL 61801, USA

ARTICLE INFO

Article history:
Received 29 August 2014
Received in revised form 18 January 2015
Accepted 20 January 2015
Available online 4 February 2015
Editor: A. Yin

Keywords:
Tibet
low-velocity zone
crustal flow
Rayleigh wave
receiver function
joint inversion

ABSTRACT

Competing geodynamic models, such as rigid-block extrusion, continuous deformation, and the mid-lower crustal flow, have been proposed to describe the growth and expansion of eastern Tibet. However, the dynamic processes responsible for plateau evolution and deformation remain poorly understood partly due to resolution limitations of previous models of lithospheric structure. On the basis of joint inversion of Rayleigh wave dispersion and receiver functions using data from a newly deployed seismic array, we have obtained a high-resolution 3D image that reveals the distribution of low-velocity zones (LVZs) with unprecedented clarity. The prominent feature of our model is two low-velocity channels that bound major strike-slip faults in SE Tibet and wrap around the Eastern Himalaya Syntaxis, consistent with the clockwise movement of crustal material in this region. Most large earthquakes in this region occurred in the boundaries of the LVZs. We propose that ductile flow within these channels, in addition to shear motion along strike-slip faults, played a significant role in accommodating intensive lithospheric deformation during the eastward expansion of Tibet in the Cenozoic.

1. Introduction

The Cenozoic collision between India and Eurasia has resulted in the shortening and thickening of the crust and growth of the Tibetan Plateau (TP) (Harrison et al., 1992; Hubbard and Shaw, 2009; Molnar and Tapponnier, 1975; Royden et al., 2008; Tapponnier et al., 2001; Yin and Harrison, 2000). Several models have been proposed to explain the deformation of the eastern TP, including: (1) lateral extrusion of rigid blocks, in which deformation is primarily localized along strike-slip faults that bound the blocks (Molnar and Tapponnier, 1975; Tapponnier et al., 1982, 2001); (2) continuous deformation, in which deformation distributes through a continuously deforming lithosphere (England and Houseman, 1986; Yang and Liu, 2013); and (3) ductile channel flow in the middle/lower crust (Clark and Royden, 2000; Royden et al., 1997; Shen et al., 2001). The mechanisms for plateau deformation and expansion have remained enigmatic due to the resolution limitations of methods and/or data. Consequently, which of the aforementioned models best describes the deformation of the eastern TP has been the subject of enduring debate.

Our study region (white box in Fig. 1) is well situated to investigate the kinematics and dynamics of plateau expansion (Copley, 2008). It comprises four main geological blocks (Fig. 2): the Yunnan–Myanmar–Thailand Block (YMTB), the Indo–China Block (ICB), the Sichuan–Yunnan Diamond Block (SYDB), and the South China Block (SCB), which are separated by the Nujiang fault (NJF), the Jingshajiang–Red River fault system (JSJF and RRF), and the Anninghe–Zemuhe–Xiaojiang fault system (ANHF, ZMHF and XJF). The Xiaojinhe fault (XJHF) divides the SYDB further into the northern and southern parts. Previous studies have suggested that the low-velocity zones (LVZs) observed in SE Tibet may be truncated at depth by faults (Chen et al., 2014; Huang et al., 2002; Wang et al., 2003; Yao et al., 2008, 2010). However, the geometric relationships between LVZs and faults remain unclear due to insufficient spatial resolution or the limited geographic extent of previous lithospheric structure models.

* Corresponding authors at: State Key Laboratory for Mineral Deposits Research, Nanjing University, Nanjing 210093, China.
E-mail addresses: xiaosun198901@gmail.com (X. Sun), goxu@nju.edu.cn (M. Xu).

http://dx.doi.org/10.1016/j.epsl.2015.01.020
0012-821X/

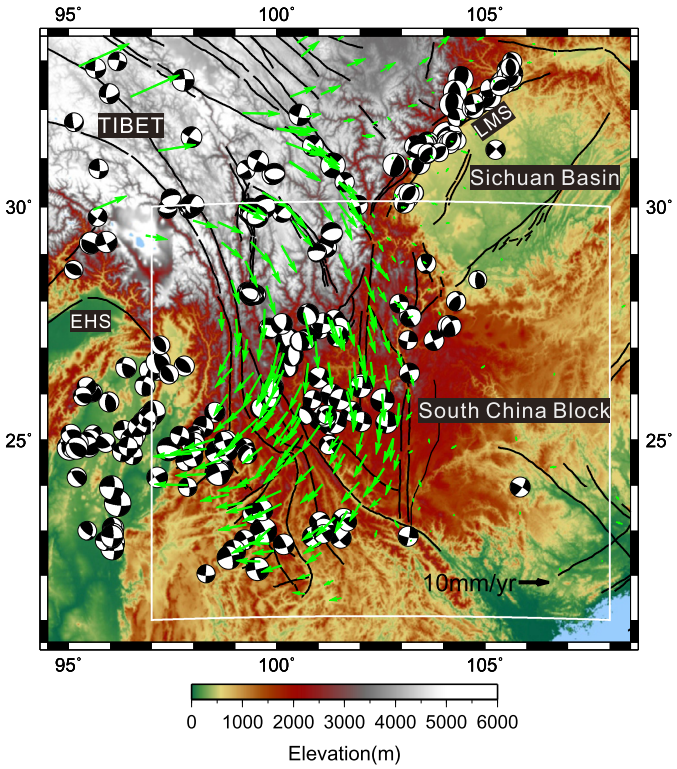

Fig. 1. Topographic map of Tibet and environments showing location of the study region (white box). Focal mechanism: from global CMT catalogue; Green arrows: GPS velocity field relative to the South China Block (Shen et al., 2005). EHS, Eastern Himalaya Syntaxis; LMS, Longmen Shan. (For interpretation of the references to color in this figure legend, the reader is referred to the web version of this article.)

In the Global Positioning System (GPS) velocity field with respect to the SCB reference frame (Fig. 1), the clockwise rotation of the SYDB around the Eastern Himalaya Syntaxis (EHS) is particularly striking, suggestive of southeastward extrusion of crustal material from the interior of the plateau due to the convergence of India with Eurasia (Gan et al., 2007; Shen et al., 2005; Zhang et al., 2004). It is not yet well understood, however, why the GPS velocity field of this region changes its direction from southward to southwestward across ~26°N, and even to westward farther south in western Yunnan. Due to the active and complex tectonic interaction of different blocks, our study region is characterized by the highest level of seismicity in Mainland China. Most earthquakes occurred along the main faults and their focal mechanism solutions are dominated by strike-slip offsets (Fig. 1). Since the 1970s, 8 large earthquakes with magnitudes ≥7.0 have occurred in this region. Most recently, on 3 August 2014, the magnitude 6.5 Ludian earthquake struck this region and caused significant casualties and damage; further understanding of the seismotectonics and crustal motion requires improved knowledge of the deep crustal structure.

In this study, we investigate LVZs beneath SE Tibet through joint inversion of P wave receiver functions and Rayleigh wave phase and group velocities. Using the newly deployed dense seismic array in SE Tibet, we seek to obtain a high-resolution three-dimensional (3D) image of crustal and upper-mantle shear-wave velocity (V_S) structure, with special attention to the detailed distribution of intra-crustal LVZs and the level of connectivity between them, since they are often regarded as diagnostic for zones of weak strength caused by the existence of fluids and/or partial melt (Liu et al., 2014; Nelson et al., 1996; Unsworth et al., 2005; Wei et al., 2001). Salient features of our models include: (1) two channels of LVZs in the mid-lower crust that wrap around the EHS, consistent with the clockwise pattern of crustal movement revealed by GPS measurements; (2) a geometric relationship in which the two channels bound with major strike-slip faults; and further that most large earthquakes in the region are located near the edge of the LVZs. These observational constraints provide fresh insights into the deformation and seismicity of SE Tibet.

2. Data

We used two independent data sets: P wave receiver functions and Rayleigh wave phase and group velocities. Receiver functions were computed from teleseismic P waveforms recorded at more than 300 temporary broadband seismic stations (Fig. 2b) from the ChinArray program during the time period from August 2011 to August 2012 in SE Tibet (Ding and Wu, 2013). These stations were deployed by the China Earthquake Administration and Nanjing University in September 2010, with an average interstation distance of ~35 km. Each station consisted of a Guralp CMG-40 or CMG-3ESP seismometer and a Reftek 130 data acquisition system. Rayleigh wave phase and group velocities at periods of 10–70 s for each station were extracted from the results of the ambient noise tomography of Mainland China, which utilized more than 1000 stations mainly from the newly updated Chinese provincial seismic networks and several PASSCAL seismic arrays in Tibet and achieved a resolution of 1° in SE Tibet (Bao et al., submitted for publication). Fig. S1 (Supplementary material) shows several representative Rayleigh wave phase velocity maps and two V_S profiles from inversion of dispersion data along 25°N and 26°N, respectively.

3. Methods

3.1. Receiver functions

We selected 545 earthquakes with good signal-to-noise ratios, magnitudes ≥5 and epicentral distances between 30° and 90° (Fig. 3), and applied the time-domain iterative deconvolution method (Ligorria and Ammon, 1999) to calculate receiver functions. The time-domain deconvolution method applies a Gaussian low-pass filter to remove high-frequency noise. For each event, we set the Gaussian parameter to a value of 2.0 (corresponding to a corner frequency of 1 Hz). To obtain reliable receiver functions, we visually checked all the receiver functions at each station by Funclab (Eagar and Fouch, 2012), and discarded bad-quality events manually. A total of 10 702 radial receiver functions were finally obtained. Figs. S2–3 display individual radial and transverse receiver functions for stations 53 065 and 53 156, respectively. Fig. S4 shows a radial receiver function profile along 25°N, which reveals clear Pms conversions below most stations and strong negative intra-crustal phase conversions west of station 52 048. In this study, we only used radial receiver functions to resolve the isotropic velocity structure although the existence of transverse energy may be suggestive of a complex structure (such as azimuthal anisotropy or dipping interface) (Figs. S2–3).

3.2. Joint inversion

Joint inversion of receiver functions and surface wave dispersion has been established as an effective way of mapping V_S structure (Gilligan et al., 2014; Julià et al., 2000; Lawrence and Wiens, 2004; Liu et al., 2014; Shen et al., 2013; Sosa et al., 2014; Xu et al., 2013b). Here, we used a linear joint inversion method (Herrmann and Ammon, 2002; Julià et al., 2000), with a starting model based on AK135 (Kennett et al., 1995), to invert for the crustal and upper mantle V_S structure in SE Tibet. Receiver functions are mainly sensitive to velocity discontinuities, whereas

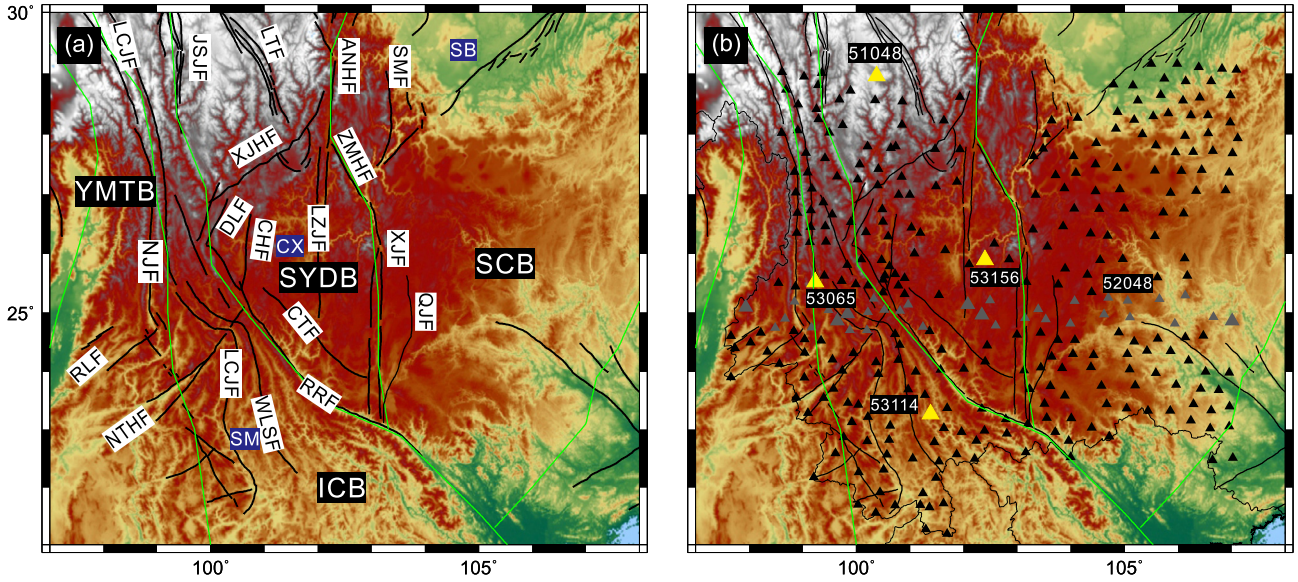

Fig. 2. (a) Geological setting. Green lines are boundaries between major blocks, and black lines represent faults in the study region. (YMTB, Yunnan–Myanmar–Thailand Block; ICB, Indo–China Block; SYDB, Sichuan–Yunnan Diamond Block; SCB, South China Block; SB, Sichuan Basin; SM, Simao Basin; CX, Chuxiong Basin; NJF, Nujiang Fault; LCJF, Lancangjiang Fault; JSJF: Jinshajiang Fault; RRF, Red River Fault; LTF, Litang Fault; XJHF, Xiaojinhe Fault; DLF, Dali Fault; CHF, Chenghai Fault; LZJF, Luzhijiang Fault; CTF, Chuxiong–Tonghai Fault; XJF, Xiaojiang fault; ZMHF, Zemuhe Fault; ANHF, Anninghe Fault; SMF, Shimian Fault; RLF, Ruili–Longling Fault; NTHF, Nantinghe Fault; WLSF, Wuliangshan Fault; QJF, Qujiang Fault.) (b) Location of the seismic array (triangles). Grey triangles are stations used to plot the receiver function profile along 25°N in Fig. S4. (For interpretation of the references to color in this figure legend, the reader is referred to the web version of this article.)

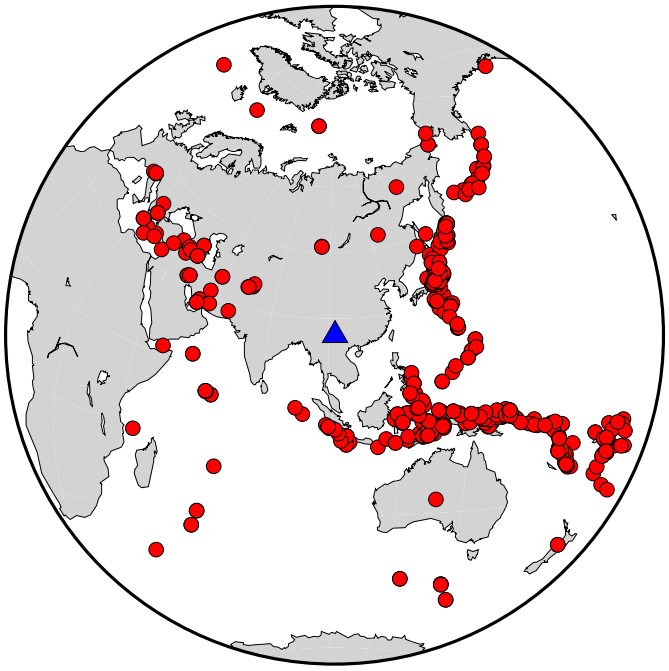

Fig. 3. Epicenters of teleseismic events for receiver functions used in this study. Red dots represent earthquakes, and the blue triangle represents the center of the seismic array. (For interpretation of the references to color in this figure legend, the reader is referred to the web version of this article.)

Rayleigh wave dispersion measurements constrain the average velocities (Bao et al., 2011b; Julià et al., 2000). The combination of receiver functions with Rayleigh wave dispersion velocities therefore provides tighter constraints on the V_S structure than either method individually (Fig. S5). We expected to obtain a better V_S model beneath SE Tibet by jointly inverting the two data sets, with Rayleigh wave dispersion recovering large-scale background velocities and receiver functions resolving small-scale velocity contrasts. Resolution tests show that joint inversion can well resolve a ~2 km thick low velocity layer with error less than 0.05 km/s (Fig. S5). Another advantage of joint inversion is that the resulting velocity models have little dependence on the starting model (Julià et al., 2000).

Since each station usually has a number of receiver functions, there are two methods to perform joint inversion, which generally produce similar results (Figs. S2–3). The first method is to resolve one velocity model to fit all individual receiver functions (Sun et al., 2014); the second approach is to stack all the receiver functions of each station to form one receiver function waveform for joint inversion (Liu et al., 2014). In this study, we used the second method to save computation time. In addition, we used a bootstrap method (Efron and Tibshirani, 1991) to evaluate the error of our velocity model. If one station has N receiver functions, we randomly selected $1.5 * N$ receiver functions from the data to produce a stacked receiver function and repeated this resampling process 500 times to generate 500 stacked receiver function traces, which were used individually for joint inversion to obtain 500 velocity models. The tests demonstrated the stability of our method and showed that the error of our velocity model is less than 0.05 km/s (Fig. S6).

We took the depth at which the vertical velocity gradient reaches a local maximum around the velocity range between the average lower-crustal and upper mantle S wave velocities, i.e., 3.8 and 4.3 km/s respectively, as the Moho. As an example, the joint inversion results for station 51 048 are displayed in Fig. 4. In this figure, we note that there are LVZs in the crust and that the predictions from the resultant model fit the observed data sets well. More examples are shown in supplementary material (Figs. S7–9).

To evaluate the robustness of the main features in our model, we performed synthetic "restoring" tests. We used the resulting 3D shear velocity model from real data as input model. After forward calculation of receiver functions and Rayleigh wave phase and group velocities, we performed joint inversion of synthetic data sets using the same scheme executed for real data. Fig. S10 shows that the velocity patterns are well recovered, although there are some minor differences between input and recovered models.

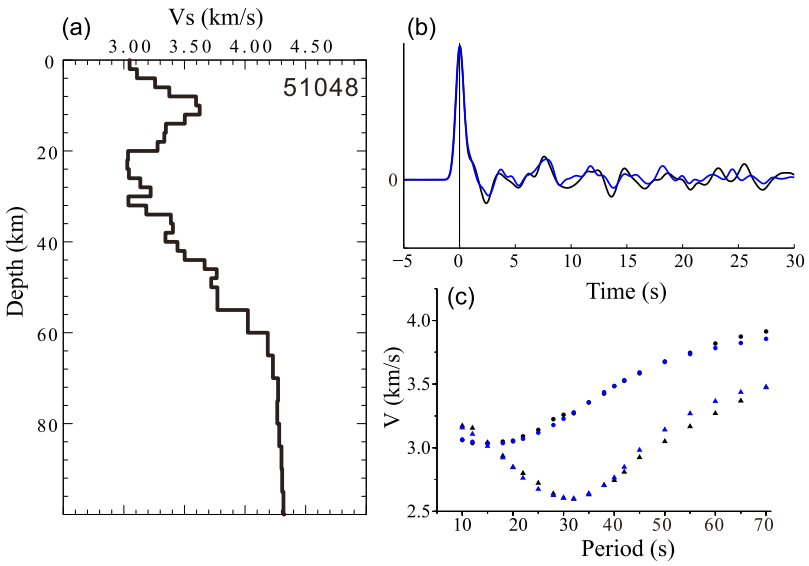

Fig. 4. (a) The inverted V_s model for station 51 048 marked in Fig. 2b. (b) Receiver function fit: observed receiver function (black curve) and predicted receiver function (blue curve). (c) The dispersion curve fits: observed phase velocities (black dots) and predicted phase velocity curves (blue dots); observed group velocities (black triangles) and predicted group velocity curves (blue triangles). (For interpretation of the references to color in this figure legend, the reader is referred to the web version of this article.)

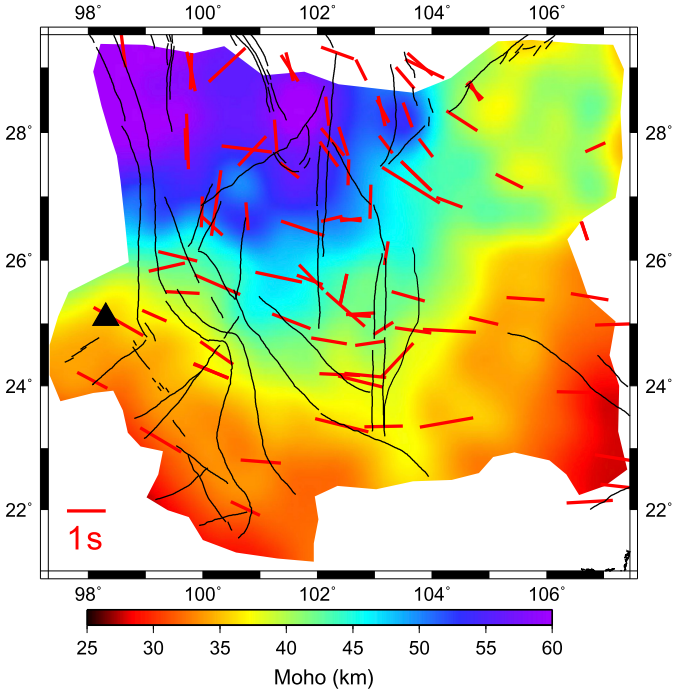

Fig. 5. Moho depths from joint inversion of receiver functions and Rayleigh wave group and phase velocities. Black triangle represents the Tengchong volcano, and short red bars give the SKS splitting results (Lev et al., 2006; Sol et al., 2007; Wang et al., 2008) with the orientation and length of each bar representing the fast direction and delay time, respectively. (For interpretation of the references to color in this figure legend, the reader is referred to the web version of this article.)

4. Results

Our joint inversion results reveal strong lateral variations of crustal thickness and V_s structure in SE Tibet. The Moho interface deepens from ~30 km in the south to ~60 km in the north of the study region (Fig. 5), which is consistent with previous estimates (Li et al., 2006; Li et al., 2014; Xu et al., 2007). Importantly, the sharp transition from thick crust to thin crust appears around 26°N, where the GPS velocity vectors (Fig. 1), the fast shear-wave polarization directions (Fig. 5) and the trends of crustal LVZs (Fig. 6) all show significant variations. The lateral variations of V_s at 3, 15, 21, 31, 41, 52.5, 67.5 and 115 km depths are depicted in Fig. 6. Several representative velocity profiles from the surface to 100 km depth are shown in Fig. 7, which displays the complex distribution of LVZs and the coincidence of the boundaries of the LVZs with major active strike-slip faults in the study region.

As shown in Fig. 6, the V_s distribution patterns show different features at different depths. At 3 km depth, the SB is characterized by low-velocity anomalies due to the presence of thick sediments, and the Tengchong volcano exhibits high V_s probably related to volcanic rocks near the surface. Other low-velocity anomalies are indicative of small sedimentary basins in this region, such as the Chuxiong basin and the Simao basin. At a depth of 15 km, the velocity pattern is characterized by pervasive LVZs with small high-velocity anomalies in-between, quite different from the shallower pattern at 3 km depth. At 21 km depth, the most conspicuous feature is two channels of LVZs (channels A and B) that appear to wrap around the EHS, in a manner that strongly resembles the clockwise movement of crustal material in this region revealed by GPS measurements (Fig. 1). Channel A extends from the northern SYDB southward across the JSJF-RRF system into the YMTB, while channel B extends from the southeastern SYDB southward across the RRF into the ICB. At 31 km depth, channels A and B terminate near the RRF and the CTF, respectively, where crustal thickness also changes significantly (Fig. 5). At 41 km depth, the velocity pattern changes again, with only one prominent continuous LVZ in the north, related to the thick crust in the north of the study region (Fig. 5). At 52.5 km depth, LVZs beneath the Tengchong volcano and the ICB may be related to upwelling asthenosphere. At a depth of 67.5 km, asthenosphere-like low-velocities appear in the YMTB, the ICB and the southern SCB, which is more conspicuous at 115 km depth, highlighting the contrasting lithospheric structure across ~26°N with thin lithosphere to the south and thick lithosphere to the north. This sharp transition of lithospheric thickness is consistent with previous result (An and Shi, 2006) and corresponds to the changes of fast shear-wave polarization directions from primarily north–south orientations in the north to nearly east–west directions in the south (Fig. 5) (Flesch et al., 2005; Lev et al., 2006; Sol et al., 2007; Wang et al., 2008), indicating different origins of the observed shear-wave splitting with lithospheric anisotropy dominated in the north (Sol et al., 2007) and asthenospheric anisotropy in the south.

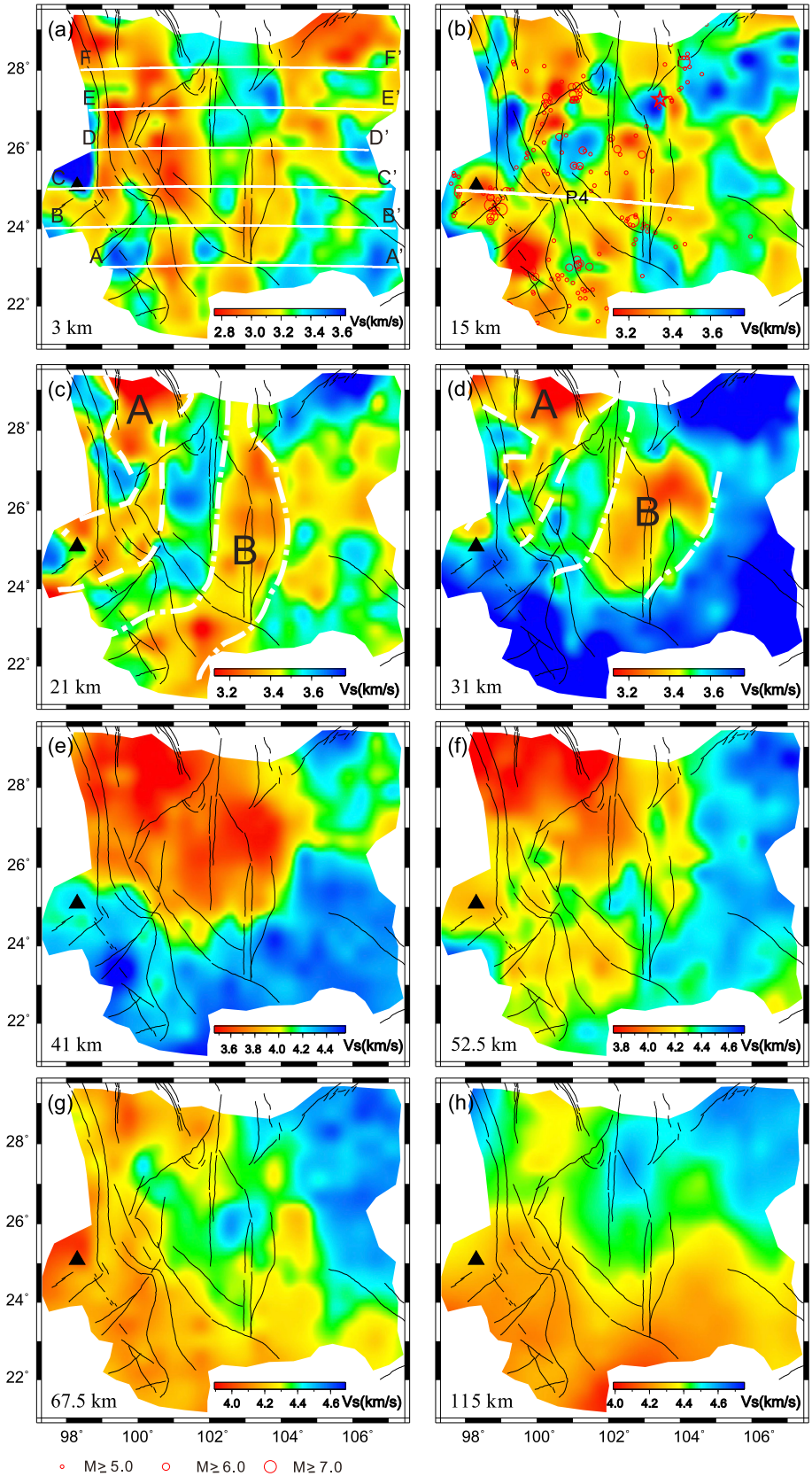

Fig. 6. V_S at 3, 15, 21, 31, 41, 52.5, 67.5 and 115 km depths. Black triangle represents the Tengchong volcano. Red circles in (b): epicentres of earthquakes (Ms > 5.0) between 1970 and 2014 (source: China Earthquake Data Center). The red star in (b) is Ludian earthquake on 3 August 2014. White dashed and dot–dashed lines in (c–d) are boundaries of two channels of LVZs (channels A and B), respectively. Lines AA′–FF′ in (a) denote locations of velocity cross sections in Fig. 7. Line P4 in (b) is the location of velocity cross section in Fig. 8. (For interpretation of the references to color in this figure legend, the reader is referred to the web version of this article.)

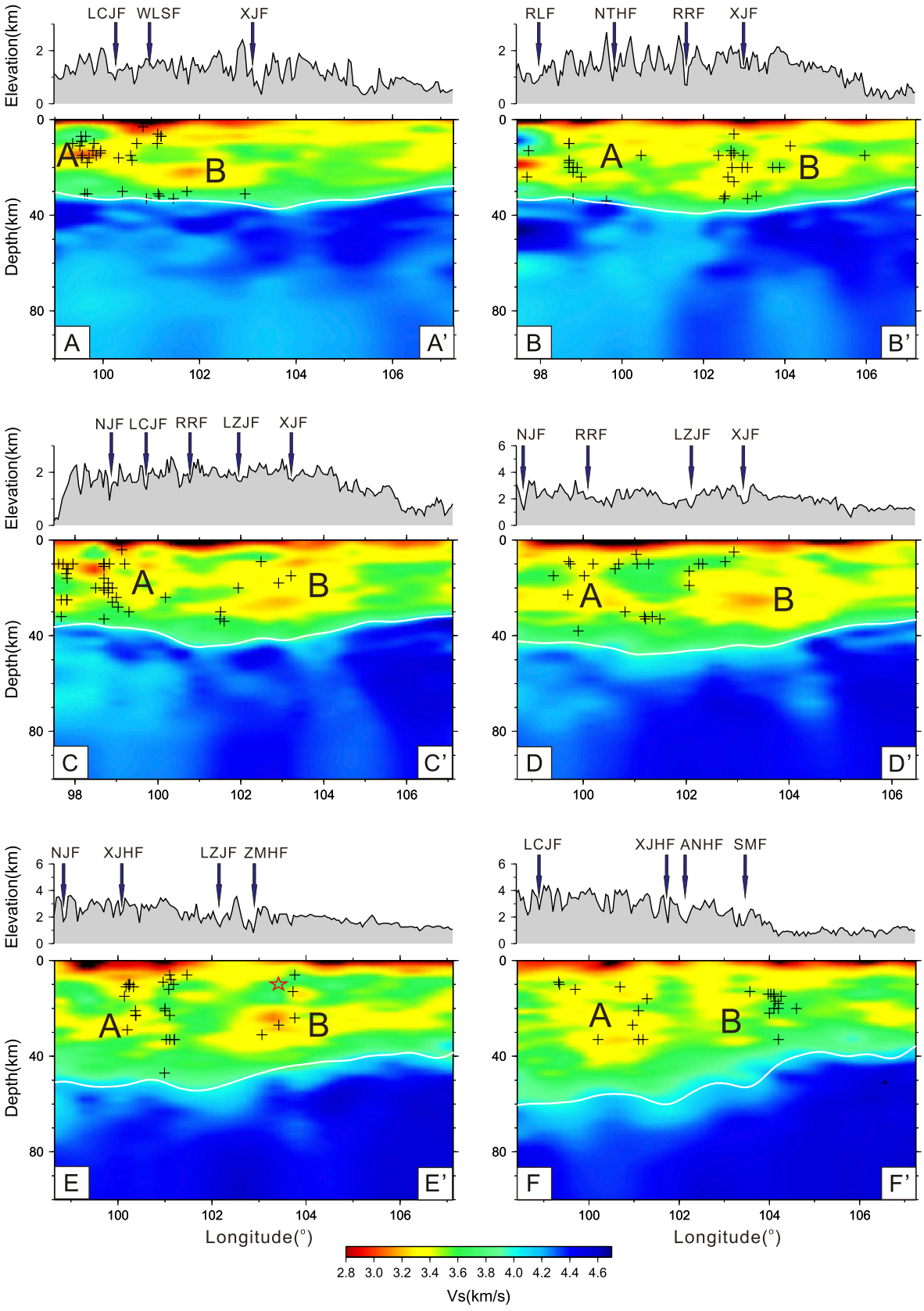

Fig. 7. Cross-sections of V_s along six profiles shown in Fig. 6a. A and B represent two channels of LVZs as shown in Figs. 6c–d. White lines represent the estimated Moho, black crosses represent earthquakes shown in Fig. 6b, and the red star in profile EE′ is Ludian earthquake on 3 August 2014. Topography is plotted above each profile. (For interpretation of the references to color in this figure legend, the reader is referred to the web version of this article.)

Fig. 7 shows V_S structure and crustal thickness along several representative profiles. Along profile AA′, it is clear that channels A and B are at different depths. Channel A, terminating adjacent to the LCJF, is at 10–20 km depth, while channel B, confined between the WLSF and the RRF, is at 20–30 km depth. As shown in profile BB′, channels A and B are somewhat diffuse, perhaps indicative of their complex interconnectivity. To the north, profiles CC′ and DD′ show that the two channels are thick, which correlates with the crustal thickening. The two profiles also illustrate that channel B is truncated by the LZJF to the west and extends across the XJF into the SCB. It is worth noting that the eastern boundary of intra-crustal LVZs on profile CC′ (~105°E is near station 52 048, west of which there are strong negative phase conversions on the receiver function profile along 25°N (Fig. S4) probably related to the LVZs, indicating the robustness of our model. Comparing profiles CC′ and DD′ from joint inversion with profiles from dispersion inversion at the same positions (Figs. S1e–f), we can find that joint inversion can better constrain the distributions of LVZs and the nature of Moho, as stated above. As shown in profile EE′, the recent Ludian earthquake (Red star) with magnitude 6.5 occurred above channel B. Far to the north, profile FF′ shows that channel A is very thick extending from 10 to 40 km depth, which probably connects to the LVZs to the north imaged previously by Liu et al. (2014). It is important to note that most large earthquakes (Black crosses) are located within the boundaries of the LVZs (Fig. 7).

5. Implications for the deformation of SE Tibet

The crustal-flow model, in which the strength of mid-lower crust is several orders of magnitude less than that of upper crust, provides a satisfactory explanation for the variations of topography and the lack of substantial young upper crustal shortening in the eastern margin of the TP (Clark and Royden, 2000; Royden et al., 1997, 2008; Shen et al., 2001). The mechanically weak mid-lower crust has also been supported by several lines of evidence from geophysical observations, such as intra-crustal LVZs (Bao et al., 2013; Ceylan et al., 2012; Fu et al., 2010; Li et al., 2008; Xu et al., 2013a; Xu and Song, 2010; Yang et al., 2012; Yao et al., 2008), low electrical resistivity in the mid-lower crust (Bai et al., 2010; Unsworth et al., 2005; Wei et al., 2001), high V_p/V_s ratios (Sun et al., 2014; Xu et al., 2007), high heat flow (Hu et al., 2000), and strong attenuation (Bao et al., 2011a; Zhao et al., 2013), indicating the existence of partial melt and viscosity reduction in the mid-lower crust and thus the possibility of crustal flow. In addition, strong positive radial anisotropy with faster horizontally polarized shear wave further suggests sub-horizontal alignment of mica and/or amphiboles in the crust due to ductile flow beneath SE Tibet (Huang et al., 2010; Shapiro et al., 2004; Xie et al., 2013).

Recent studies suggest that there may exist two channels of crustal flow in SE Tibet (Bai et al., 2010; Sun et al., 2014; Zhao et al., 2013). On the basis of magnetotelluric images, Bai et al. (2010) observed two channels of high conductivity at depths of 20–40 km in east Tibet, which they interpreted as distinct channels of crustal flow. A complex pattern of crustal flow was also suggested by regional Lg-wave attenuation tomography (Zhao et al., 2013), which revealed two belts of high attenuation in Tibet. In our previous work (Sun et al., 2014), two intra-crustal LVZs were imaged along a ~25°N latitude profile in SE Tibet through joint inversion of Rayleigh wave dispersion and receiver functions. Using ambient-noise adjoint tomography, Chen et al. (2014) also observed disconnected channels of LVZs in SE Tibet. Fig. 8 compares the distributions of high conductivity layer (Bai et al., 2010), Q_{Lg} (Zhao et al., 2013) and LVZs from our model along the P4 profile (Fig. 6b) in Bai et al. (2010). We can see that the two high conductivity layers imaged by Bai et al. (2010) are generally within

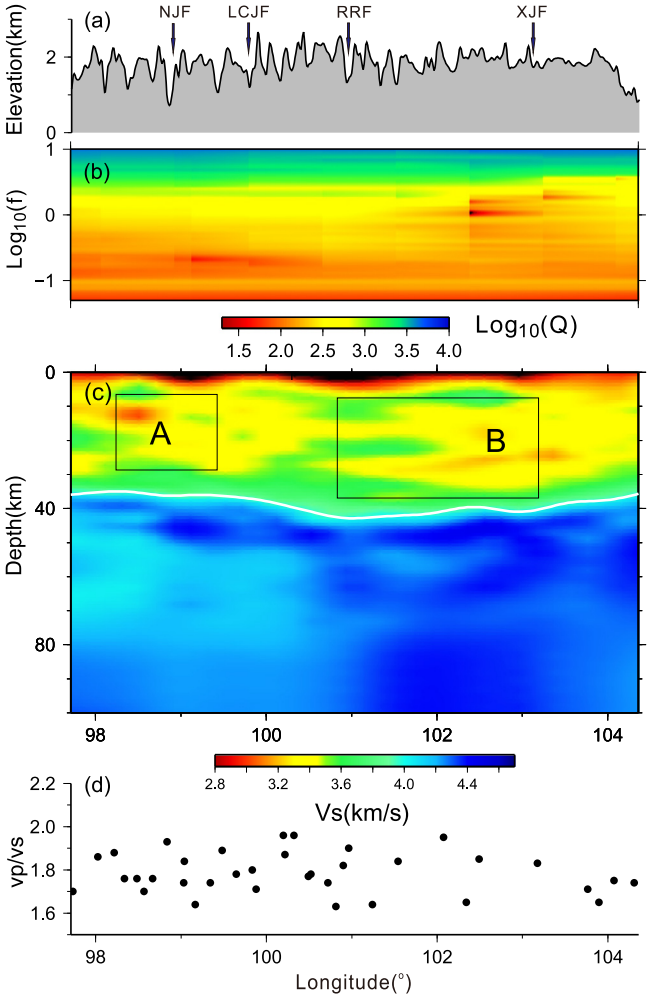

Fig. 8. Topography (a), log(Q_{Lg}) versus frequency (b), and V_s (c) along P4 profile shown in Fig. 6b. A and B in (c) are two channels of LVZs, and the two rectangles represent the high conductivity layers imaged by Bai et al. (2010). (d) V_p/V_s ratios along ~25°N from Sun et al. (2014).

the two channels of LVZs in our model and that channel B roughly correlates with one belt of low Q_{Lg} (or high attenuation) detected by Zhao et al. (2013), likely indicating the presence of partial melt in the LVZs. However, channel A is to the east of the other belt of high attenuation, which may be caused by the lower resolution for the other belt of low Q_{Lg} due to the relatively sparse path coverage in that area. Crustal average V_p/V_s ratios along a nearby profile (Sun et al., 2014) are shown in Fig. 8d, which reveals high average V_p/V_s ratios to the west of the XJF. Although the LVZ to the east of the XJF is featured by normal V_p/V_s ratios, it is still correlated to both high attenuation and strong positive radial anisotropy (Xie et al., 2013).

Due to limited profiles or resolution, previous results do not adequately constrain the spatial extent of the two inferred channels of crustal flow and their relationships with surface motion and main faults on a broad region. The high density of teleseismic data in SE Tibet enables us to investigate the lithospheric structure of this region with unprecedented resolution. Our model shows that the two channels of LVZs (channels A and B in Figs. 6–7) in the mid-lower crust wrap around the EHS and bound major strike-slip faults in SE Tibet, such as the JSJF, the XJF, and the LZJF. Channels A and B are accompanied by the occurrence of high electrical conductivity (Bai et al., 2010), strong attenuation (Zhao et al., 2013) and positive radial anisotropy (Huang et al., 2010; Xie et al., 2013), suggesting that they probably represent mechanically weak mate-

rials, which would facilitate ductile flow on a geological timescale driven by gravitational potential energy (Clark and Royden, 2000; Copley, 2008). The coincidence of the direction of crustal motion (Fig. 1) and the trends of channels A and B (Fig. 6) indicates that the curvature of the two channels probably contributes to the clockwise rotation of upper crustal movement in this region. The overlap of the main strike-slip faults and the boundaries of channels A and B revealed here may point to a close relationship between LVZs and shear deformation. For example, the shear heating caused by relative movements between different blocks along strike-slip faults may contribute to reduce mid-lower crustal viscosity and velocity and thus the formation of intra-crustal LVZs (Leloup et al., 1999). On the other hand, LVZs with lower viscosity would facilitate the relative motions of rigid upper crustal blocks, making the moving of the strike-slip faults less resistant. Taken together we suggest that the growth and expansion of SE Tibet was accommodated by a combination of two channels of crustal flow and shearing of strike-slip faults. Some previous studies also pointed out the importance of both crustal flow and strike-slip faulting for the deformation of SE Tibet (Liu et al., 2014; Yao et al., 2008, 2010).

The complex crustal heterogeneity imaged here has potential significance for understanding seismic hazards in SW China. The combination of crustal flow and boundary shearing provides new insights into the intensive regional seismicity. As shown in Fig. 7, most large earthquakes in this region occurred in the boundary zones of channels A and B. This relationship suggests that although earthquakes mostly occur in the upper to middle crust, the existence of the LVZs may facilitate the motion of the faults, thus the deformation at depth in the two channels may play a key role in seismogenesis in the region.

6. Conclusions

In this study, we obtain a high-resolution V_S model of the lithosphere under SE Tibet using the newly deployed dense seismic array, through joint inversion of receiver functions and Rayleigh wave dispersion. Our model provides constraints on the complex distributions of two channels of crustal LVZs in SE Tibet. The striking features of the two channels are as follows: (1) channels A and B wrap around the EHS and bound with main strike-slip faults in SE Tibet, consistent with the clockwise movement of crustal material; and (2) most large earthquakes occurred in the boundary zones of the two channels. The new information about the distribution of LVZs gives significant insights into the deformation and seismicity of SE Tibet. We suggest that both ductile flow and shearing along strike-slip faults play an import role in accommodating lithospheric deformation during the uplift and expansion of eastern Tibet.

Acknowledgements

We thank two anonymous reviewers for their constructive and critical comments and Dr. Lianfeng Zhao for providing the Lg-wave attenuation data used in Fig. 8b. This study was supported by China National Special Fund for Earthquake Scientific Research in Public Interest (201308011 and 201008001), China Postdoctoral Science Foundation funded project (2012M521046), Key Laboratory of Seismic Observation and Geophysical Imaging (SOGI 2013 FUDA01), and the Natural Science Foundation of China (41274056). The waveform data was provided by China Seismic Array Data Management Center at Institute of Geophysics, China Earthquake Administration. Most figures were prepared using Generic Mapping Tools (GMT) (Wessel and Smith, 1998).

Appendix A. Supplementary material

Supplementary material related to this article can be found online at http://dx.doi.org/10.1016/j.epsl.2015.01.020.

References

An, M.J., Shi, Y.L., 2006. Lithospheric thickness of the Chinese continent. Phys. Earth Planet. Inter. 159, 257–266.
Bai, D., Unsworth, M.J., Meju, M.A., Ma, X., Teng, J., Kong, X., Sun, Y., Sun, J., Wang, L., Jiang, C., Zhao, C., Xiao, P., Liu, M., 2010. Crustal deformation of the eastern Tibetan Plateau revealed by magnetotelluric imaging. Nat. Geosci. 3, 358–362.
Bao, X., Sandvol, E., Ni, J., Hearn, T., Chen, Y.J., Shen, Y., 2011a. High resolution regional seismic attenuation tomography in eastern Tibetan Plateau and adjacent regions. Geophys. Res. Lett. 38, L16304.
Bao, X., Song, X., Li, J., submitted for publication. High-resolution lithospheric structure beneath Mainland China from ambient noise and earthquake surface-wave tomography. Earth Planet. Sci. Lett.
Bao, X., Song, X., Xu, M., Wang, L., Sun, X., Mi, N., Yu, D., Li, H., 2013. Crust and upper mantle structure of the North China Craton and the NE Tibetan Plateau and its tectonic implications. Earth Planet. Sci. Lett. 369–370, 129–137.
Bao, X., Xu, M., Wang, L., Mi, N., Yu, D., Li, H., 2011b. Lithospheric structure of the Ordos Block and its boundary areas inferred from Rayleigh wave dispersion. Tectonophysics 499, 132–141.
Ceylan, S., Ni, J., Chen, J.Y., Zhang, Q., Tilmann, F., Sandvol, E., 2012. Fragmented Indian plate and vertically coherent deformation beneath eastern Tibet. J. Geophys. Res. 117, B11303.
Chen, M., Huang, H., Yao, H., van der Hilst, R., Niu, F., 2014. Low wave speed zones in the crust beneath SE Tibet revealed by ambient noise adjoint tomography. Geophys. Res. Lett. 2013GL058476.
Clark, M.K., Royden, L.H., 2000. Topographic ooze: building the eastern margin of Tibet by lower crustal flow. Geology 28, 703–706.
Copley, A., 2008. Kinematics and dynamics of the southeastern margin of the Tibetan Plateau. Geophys. J. Int. 174, 1081–1100.
Ding, Z., Wu, Z., 2013. Advances of ChinArray program. AGU, San Francisco, CA. Paper presented at 2013 AGU Fall Meeting.
Eagar, K.C., Fouch, M.J., 2012. FuncLab: a MATLAB Interactive Toolbox for handling receiver function datasets. Seismol. Res. Lett. 83, 596–603.
Efron, B., Tibshirani, R., 1991. Statistical data analysis in the computer age. Science 253, 390–395.
England, P., Houseman, G., 1986. Finite strain calculations of continental deformation. 2. Comparison with the India–Asia collision zone. J. Geophys. Res. 91, 3664–3676.
Flesch, L., Holt, W., Silver, P., Stephenson, M., Wang, C., Chan, W., 2005. Constraining the extent of crust–mantle coupling in central Asia using GPS, geologic, and shear wave splitting data. Earth Planet. Sci. Lett. 238, 248–268.
Fu, Y.V., Li, A., Chen, Y.J., 2010. Crustal and upper mantle structure of southeast Tibet from Rayleigh wave tomography. J. Geophys. Res. 115, B12323.
Gan, W., Zhang, P., Shen, Z.-K., Niu, Z., Wang, M., Wan, Y., Zhou, D., Cheng, J., 2007. Present-day crustal motion within the Tibetan Plateau inferred from GPS measurements. J. Geophys. Res. 112, B08416.
Gilligan, A., Roecker, S.W., Priestley, K.F., Nunn, C., 2014. Shear velocity model for the Kyrgyz Tien Shan from joint inversion of receiver function and surface wave data. Geophys. J. Int. 199, 480–498.
Harrison, T.M., Copeland, P., Kidd, W.S.F., Yin, A., 1992. Raising Tibet. Science 255, 1663–1670.
Herrmann, R.B., Ammon, C.J., 2002. Computer Programs in Seismology: Surface Wave, Receiver Function and Crustal Structure. Saint Louis University, St. Louis, MO, USA.
Hu, S.B., He, L.J., Wang, J.Y., 2000. Heat flow in the continental area of China: a new data set. Earth Planet. Sci. Lett. 179, 407–419.
Huang, H., Yao, H., van der Hilst, R.D., 2010. Radial anisotropy in the crust of SE Tibet and SW China from ambient noise interferometry. Geophys. Res. Lett. 37, L21310.
Huang, J.L., Zhao, D.P., Zheng, S.H., 2002. Lithospheric structure and its relationship to seismic and volcanic activity in southwest China. J. Geophys. Res. 107, 2255.
Hubbard, J., Shaw, J.H., 2009. Uplift of the Longmen Shan and Tibetan Plateau, and the 2008 Wenchuan (M = 7.9) earthquake. Nature 458, 194–197.
Julià, J., Ammon, C.J., Herrmann, R.B., Correig, A.M., 2000. Joint inversion of receiver function and surface wave dispersion observations. Geophys. J. Int. 143, 99–112.
Kennett, B.L.N., Engdahl, E.R., Buland, R., 1995. Constraints on seismic velocities in the Earth from travel-times. Geophys. J. Int. 122, 108–124.
Lawrence, J.F., Wiens, D.A., 2004. Combined receiver-function and surface wave phase-velocity inversion using a Niching Genetic Algorithm: application to Patagonia. Bull. Seismol. Soc. Am. 94, 977–987.
Leloup, P.H., Ricard, Y., Battaglia, J., Lacassin, R., 1999. Shear heating in continental strike-slip shear zones: model and field examples. Geophys. J. Int. 136, 19–40.
Lev, E., Long, M., Vanderhilst, R., 2006. Seismic anisotropy in Eastern Tibet from shear wave splitting reveals changes in lithospheric deformation. Earth Planet. Sci. Lett. 251, 293–304.

Li, Y., Gao, M., Wu, Q., 2014. Crustal thickness map of the Chinese mainland from teleseismic receiver functions. Tectonophysics 611, 51–60.
Li, S., Mooney, W.D., Fan, J., 2006. Crustal structure of mainland China from deep seismic sounding data. Tectonophysics 420, 239–252.
Li, Y., Wu, Q., Zhang, R., Tian, X., Zeng, R., 2008. The crust and upper mantle structure beneath Yunnan from joint inversion of receiver functions and Rayleigh wave dispersion data. Phys. Earth Planet. Inter. 170, 134–146.
Ligorria, J.P., Ammon, C.J., 1999. Iterative deconvolution and receiver-function estimation. Bull. Seismol. Soc. Am. 89, 1395–1400.
Liu, Q.Y., van der Hilst, R.D., Li, Y., Yao, H.J., Chen, J.H., Guo, B., Qi, S.H., Wang, J., Huang, H., Li, S.C., 2014. Eastward expansion of the Tibetan Plateau by crustal flow and strain partitioning across faults. Nat. Geosci. 7, 361–365.
Molnar, P., Tapponnier, P., 1975. Cenozoic tectonics of Asia – effects of a continental collision. Science 189, 419–426.
Nelson, K.D., Zhao, W., Brown, L.D., Kuo, J., Che, J., Liu, X., Klemperer, S.L., Makovsky, Y., Meissner, R., Mechie, J., Kind, R., Wenzel, F., Ni, J., Nabelek, J., Leshou, C., Tan, H., Wei, W., Jones, A.G., Booker, J., Unsworth, M., Kidd, W.S.F., Hauck, M., Alsdorf, D., Ross, A., Cogan, M., Wu, C., Sandvol, E., Edwards, M., 1996. Partially molten middle crust beneath Southern Tibet: synthesis of project INDEPTH results. Science 274, 1684–1688.
Royden, L.H., Burchfiel, B.C., King, R.W., Wang, E., Chen, Z., Shen, F., Liu, Y., 1997. Surface deformation and lower crustal flow in Eastern Tibet. Science 276, 788–790.
Royden, L.H., Burchfiel, B.C., van der Hilst, R.D., 2008. The geological evolution of the Tibetan Plateau. Science 321, 1054–1058.
Shapiro, N.M., Ritzwoller, M.H., Molnar, P., Levin, V., 2004. Thinning and flow of Tibetan crust constrained by seismic anisotropy. Science 305, 233–236.
Shen, Z.-K., Lü, J., Wang, M., Bürgmann, R., 2005. Contemporary crustal deformation around the southeast borderland of the Tibetan Plateau. J. Geophys. Res. 110, B11409.
Shen, W., Ritzwoller, M.H., Schulte-Pelkum, V., Lin, F.-C., 2013. Joint inversion of surface wave dispersion and receiver functions: a Bayesian Monte-Carlo approach. Geophys. J. Int. 192, 807–836.
Shen, F., Royden, L.H., Burchfiel, B.C., 2001. Large-scale crustal deformation of the Tibetan Plateau. J. Geophys. Res. 106, 6793–6816.
Sol, S., Meltzer, A., Bürgmann, R., van der Hilst, R.D., King, R., Chen, Z., Koons, P.O., Lev, E., Liu, Y.P., Zeitler, P.K., Zhang, X., Zhang, J., Zurek, B., 2007. Geodynamics of the southeastern Tibetan Plateau from seismic anisotropy and geodesy. Geology 35, 563–566.
Sosa, A., Thompson, L., Velasco, A.A., Romero, R., Herrmann, R.B., 2014. 3-D structure of the Rio Grande Rift from 1-D constrained joint inversion of receiver functions and surface wave dispersion. Earth Planet. Sci. Lett. 402, 127–137.
Sun, X., Bao, X., Xu, M., Eaton, D.W., Song, X., Wang, L., Ding, Z., Mi, N., Yu, D., Li, H., 2014. Crustal structure beneath SE Tibet from joint analysis of receiver functions and Rayleigh wave dispersion. Geophys. Res. Lett. 41. 2014GL059269.
Tapponnier, P., Peltzer, G., Le Dain, A.Y., Armijo, R., Cobbold, P., 1982. Propagating extrusion tectonics in Asia: new insights from simple experiments with plasticine. Geology 10, 611–616.
Tapponnier, P., Zhiqin, X., Roger, F., Meyer, B., Arnaud, N., Wittlinger, G., Jingsui, Y., 2001. Oblique stepwise rise and growth of the Tibet Plateau. Science 294, 1671–1677.
Unsworth, M.J., Jones, A.G., Wei, W., Marquis, G., Gokarn, S.G., Spratt, J.E., 2005. Crustal rheology of the Himalaya and Southern Tibet inferred from magnetotelluric data. Nature 438, 78–81.
Wang, C.-Y., Chan, W.W., Mooney, W.D., 2003. Three-dimensional velocity structure of crust and upper mantle in southwestern China and its tectonic implications. J. Geophys. Res. 108, 2442.
Wang, C.-Y., Flesch, L.M., Silver, P.G., Chang, L.-J., Chan, W.W., 2008. Evidence for mechanically coupled lithosphere in central Asia and resulting implications. Geology 36, 363–366.
Wei, W., Unsworth, M., Jones, A., Booker, J., Tan, H., Nelson, D., Chen, L., Li, S., Solon, K., Bedrosian, P., Jin, S., Deng, M., Ledo, J., Kay, D., Roberts, B., 2001. Detection of widespread fluids in the Tibetan crust by magnetotelluric studies. Science 292, 716–719.
Wessel, P., Smith, W.H.F., 1998. New, improved version of generic mapping tools released. Eos 79, 579. http://dx.doi.org/10.1029/98EO00426.
Xie, J., Ritzwoller, M.H., Shen, W., Yang, Y., Zheng, Y., Zhou, L., 2013. Crustal radial anisotropy across Eastern Tibet and the Western Yangtze Craton. J. Geophys. Res. 118, 4226–4252.
Xu, L., Rondenay, S., van der Hilst, R.D., 2007. Structure of the crust beneath the southeastern Tibetan Plateau from teleseismic receiver functions. Phys. Earth Planet. Inter. 165, 176–193.
Xu, Z.J., Song, X., 2010. Joint inversion for crustal and Pn velocities and Moho depth in Eastern Margin of the Tibetan Plateau. Tectonophysics 491, 185–193.
Xu, Z., Song, X., Zheng, S., 2013a. Shear velocity structure of crust and uppermost mantle in China from surface wave tomography using ambient noise and earthquake data. Earthq. Sci. 26 (5), 267–281.
Xu, Z.J., Song, X., Zhu, L., 2013b. Crustal and uppermost mantle S velocity structure under Hi-CLIMB seismic array in central Tibetan Plateau from joint inversion of surface wave dispersion and receiver function data. Tectonophysics 584, 209–220.
Yang, Y., Liu, M., 2013. The Indo–Asian continental collision: a 3-D viscous model. Tectonophysics 606, 198–211.
Yang, Y., Ritzwoller, M.H., Zheng, Y., Shen, W., Levshin, A.L., Xie, Z., 2012. A synoptic view of the distribution and connectivity of the mid-crustal low velocity zone beneath Tibet. J. Geophys. Res. 117, B04303.
Yao, H., Beghein, C., van der Hilst, R.D., 2008. Surface wave array tomography in SE Tibet from ambient seismic noise and two-station analysis – II. Crustal and upper-mantle structure. Geophys. J. Int. 173, 205–219.
Yao, H., van der Hilst, R.D., Montagner, J.-P., 2010. Heterogeneity and anisotropy of the lithosphere of SE Tibet from surface wave array tomography. J. Geophys. Res. 115, B12307.
Yin, A., Harrison, T.M., 2000. Geologic evolution of the Himalayan–Tibetan orogen. Annu. Rev. Earth Planet. Sci. 28, 211–280.
Zhang, P.-Z., Shen, Z., Wang, M., Gan, W., Bürgmann, R., Molnar, P., Wang, Q., Niu, Z., Sun, J., Wu, J., Hanrong, S., Xinzhao, Y., 2004. Continuous deformation of the Tibetan Plateau from global positioning system data. Geology 32, 809–812.
Zhao, L.-F., Xie, X.-B., He, J.-K., Tian, X., Yao, Z.-X., 2013. Crustal flow pattern beneath the Tibetan Plateau constrained by regional Lg-wave Q tomography. Earth Planet. Sci. Lett. 383, 113–122.